Acta Pharmaceutica Sinica B 2025;15(1):627−641

Chinese Pharmaceutical Association
Institute of Materia Medica, Chinese Academy of Medical Sciences

Acta Pharmaceutica Sinica B

www.elsevier.com/locate/apsb
www.sciencedirect.com

ORIGINAL ARTICLE

In situ tumor cell engineering reverses immune escape to enhance immunotherapy effect

Shujun Liu[a,†], Shijun Yuan[a,†], Meichen Liu[a], Jinhu Liu[a], Shunli Fu[a], Tong Gao[a], Shuang Liang[a], Xinyan Huang[a], Xinke Zhang[c], Yongjun Liu[a], Zipeng Zhang[b,*], Na Zhang[a,*]

[a]*Department of Pharmaceutics, Key Laboratory of Chemical Biology (Ministry of Education), NMPA Key Laboratory for Technology Research and Evaluation of Drug Products, School of Pharmaceutical Sciences, Cheeloo College of Medicine, Shandong University, Jinan 250012, China*
[b]*Medical Science and Technology Innovation Center, Shandong First Medical University & Shandong Academy of Medical Sciences, Jinan 250062, China*
[c]*Department of Pharmacology, Key Laboratory of Chemical Biology (Ministry of Education), School of Pharmaceutical Sciences, Cheeloo College of Medicine, Shandong University, Jinan 250012, China*

Received 6 May 2024; received in revised form 10 August 2024; accepted 12 August 2024

KEY WORDS

Tumor engineering;
MHC-I;
T cell recognition;
CD55;
ICOSL$^+$ B cell;
Immunotherapy;
Immunogenic cell death;
CAR-T therapy

Abstract The underlying cause of low response rates to existing immunotherapies is that tumor cells dominate tumor immune escape through surface antigen deficiency and inducing tumor immunosuppressive microenvironment (TIME). Here, we proposed an *in situ* tumor cell engineering strategy to disrupt tumor immune escape at the root by restoring tumor cell MHC-I/tumor-specific antigen complex (MHC-I/TSA) expression to promote T-cell recognition and by silencing tumor cell CD55 to increase the ICOSL$^+$ B-cell proportion and reverse the TIME. A doxorubicin (DOX) and dual-gene plasmid (MAC pDNA, encoding both MHC-I/ASMTNMELM and CD55-shRNA) coloaded drug delivery system (LCPN@ACD) with tumor targeting and charge/size dual−conversion properties was prepared. LCPN@ACD-induced ICD promoted DC maturation and enhanced T-cell activation and infiltration. LCPN@ACD enabled effective expression of MHC-I/TSA on tumor cells, increasing the ability of tumor cell recognition and killing. LCPN@ACD downregulated tumor cell CD55 expression, increased the proportion of ICOSL$^+$ B cells and CTLs, and reversed the TIME, thus greatly improving the efficacy of αPD-1 and CAR-T therapies. The application of this *in situ* tumor cell engineering strategy eliminated the source of tumor immune escape, providing new ideas for solving the challenges of clinical immunotherapy.

*Corresponding authors.
E-mail addresses: zhangzipeng@sdfmu.edu.cn (Zipeng Zhang), zhangnancy9@sdu.edu.cn (Na Zhang).
[†]These authors made equal contributions to this work.
Peer review under the responsibility of Chinese Pharmaceutical Association and Institute of Materia Medica, Chinese Academy of Medical Sciences.

https://doi.org/10.1016/j.apsb.2024.08.028

1. Introduction

Immunotherapy has sparked a revolutionary shift in tumor treatment, in which immune checkpoint inhibitors and chimeric antigen receptor T-cell (CAR-T) therapies have achieved remarkable clinical success[1,2]. Nevertheless, tumor immunotherapy still falls far short of expectations, especially in the treatment of solid tumors. For example, very few patients show a complete response to immune checkpoint inhibitors[3,4], and CAR-T therapies are currently available only for hematologic tumors and remain suboptimal in solid tumors[5-7]. These problems are mainly attributed to tumor immune escape through tumor cell surface antigen deficiency and overexpression of certain cytokines/receptors, regulating the tumor immunosuppressive microenvironment (TIME). Although many studies have been performed to overcome tumor immune escape by focusing on regulating immunosuppressive cells or editing T cells, however, it is the tumor cell that is the root who dominates the occurrence of immune escape. Tumor cells can change and maintain the microenvironment to promote their survival and development, regulate immune cells to an immunosuppressive subtype, and restrict immune cell infiltration, thus promoting tumor growth and development[8,9]. Therefore, the direct engineering of tumor cells is expected to cut off the source of immune escape and achieve multifaceted promotion of T-cell-based immune responses.

Tumor cells exhibit insufficient antigen expression and presentation, which hinders T-cell activation and recognition, making it difficult for T cells to achieve the desired therapeutic effect[10,11]. Previous studies have focused on this issue, for example, by restoring the surface level of MHC-I to improve antigen presentation and increase tumor sensitivity to immunotherapy[12-14] or by constructing dual (multi)-target CAR-T cells to expand CAR-T-cell recognition exploiting the complementary nature of different antigens[15]. Tumors are deficient in expressing both antigens and MHC-I, which may prevent existing strategies from achieving the desired therapeutic effect. Therefore, there is an urgent need to simultaneously increase the expression of MHC-I/antigen complex (express only antigen for CAR-T therapy) to tag tumor cells and restore T cell recognition.

The tumor cells induced TIME is another major obstacle to immunotherapy[16,17]. Numerous studies have confirmed that tumor cells dominate the interaction between tumor cells and immune cells in the TIME. For example, tumor cells can regulate the phenotype of tumor-associated macrophages (TAMs) through lactate secretion, and regulate T-cell status through TGF-β[18]. TAMs, T cells, and B cells are the main immune cells in TIME[19-21]. A growing number of studies highlight the importance of B cells in TIME formation[22-24]. As reported, B cells in the TIME promote M2 macrophage differentiation and inhibit effector T-cell function by GABA secretion. Tumor cells induce B cells to adopt the tumor-promoting phenotype (Breg) to strengthen Treg- and MDSC-mediated immune suppression[25]. Previously, our group relieved the TIME by whole tumor-infiltrating B-cell depletion[26]. However, B-cell function is heterogeneous, and modulating specific B-cell subtypes may lead to new advances in immunotherapy. The ICOSL-positive subtype of B cells in TIME is considered to be tumor suppressive, which improves tumor-specific T cell responses through ICOSL/ICOS engagement, limits IL-10 production, and reduces regulatory T cells (Tregs). However, tumor CD55, a complement inhibitory protein expressed on the tumor cell membrane, significantly hindered the generation of $ICOSL^+$ B cells by inactivating complement C3 convertase[22,27]. Therefore, downregulating tumor cell CD55 to increase the proportion of $ICOSL^+$ B cells is expected to reverse the TIME. In addition, it is worth mentioning that some chemotherapy drugs, such as doxorubicin (DOX), oxaliplatin, and paclitaxel, have a positive effect on immunotherapy. It has been demonstrated that a low dose of DOX can induce immunogenic cell death (ICD) to regulate the immune microenvironment and promote the activation of T cells[28].

In this study, we reformed tumor cells with an *in situ* tumor cell engineering strategy to restore T-cell recognition by overexpressing the MHC-I/tumor-specific antigen complex (MHC-I/TSA) on tumor cell surface, to increase the proportion of $ICOSL^+$ B cells and ameliorate the TIME by downregulating tumor cell CD55 expression (Fig. 1). A dual-gene plasmid (MAC pDNA) was constructed to express MHC-I/ASMTNMELM (ASMTNMELM is a valid peptide in ADPGK (TSA of colon cancer) that binds to MHC-I[18]) and to transcribe CD55-shRNA for CD55 silencing. Cationic liposomes loaded with MAC pDNA and DOX were prepared (LNP@ACD) by the thin film dispersion method. CMCS-PEG-NGR was assembled with LNP@ACD to form LCPN@ACD, which featured tumor targeting and charge/size dual conversion to achieve tumor accumulation and deep penetration. LNP@ACD was released from LCPN@ACD in a slightly acidic TIME, readily initialized by tumor cells. MAC pDNA expressed MCH-I/TSA, which could be located on the surface of tumor cells, promoting the recognition of effector T cells. Moreover, MAC pDNA transcribed CD55 shRNA to silence tumor cell CD55, which in turn promoted $ICOSL^+$ B-cell production and reversed the TIME. A low dose of DOX could induce ICD, thus promoting DC maturation, T-cell activation, and T-cell infiltration. In summary, the tumor immune escape was thoroughly reversed, which greatly enhanced the immunotherapeutic effect of aPD-1 and CAR-T cells. The therapeutic strategy proposed in this study is universal and theoretically applicable to most of the T cells involving immunotherapies (including immune blockade therapy, adoptive cell therapy, tumor vaccines, etc.), and may provide new inspiration for immunotherapy.

2. Materials and methods

2.1. Materials

Doxorubicin hydrochloride (DOX) was obtained from Meilunbio (Dalian, China). Multi-genotype plasmids were purchased from VectorBuilder Inc. (Guangzhou, China). Carboxymethyl chitosan (CMCS) was from Macklin Inc. (Shanghai, China). NHS-PEG_{2000}-MAL was obtained from AVT Pharmaceutical Co., Ltd. (Shanghai, China). Hoechst 33342 was purchased from Shandong Sparkjade Biotechnology Co., Ltd. (Jinan, China). ICD antibodies

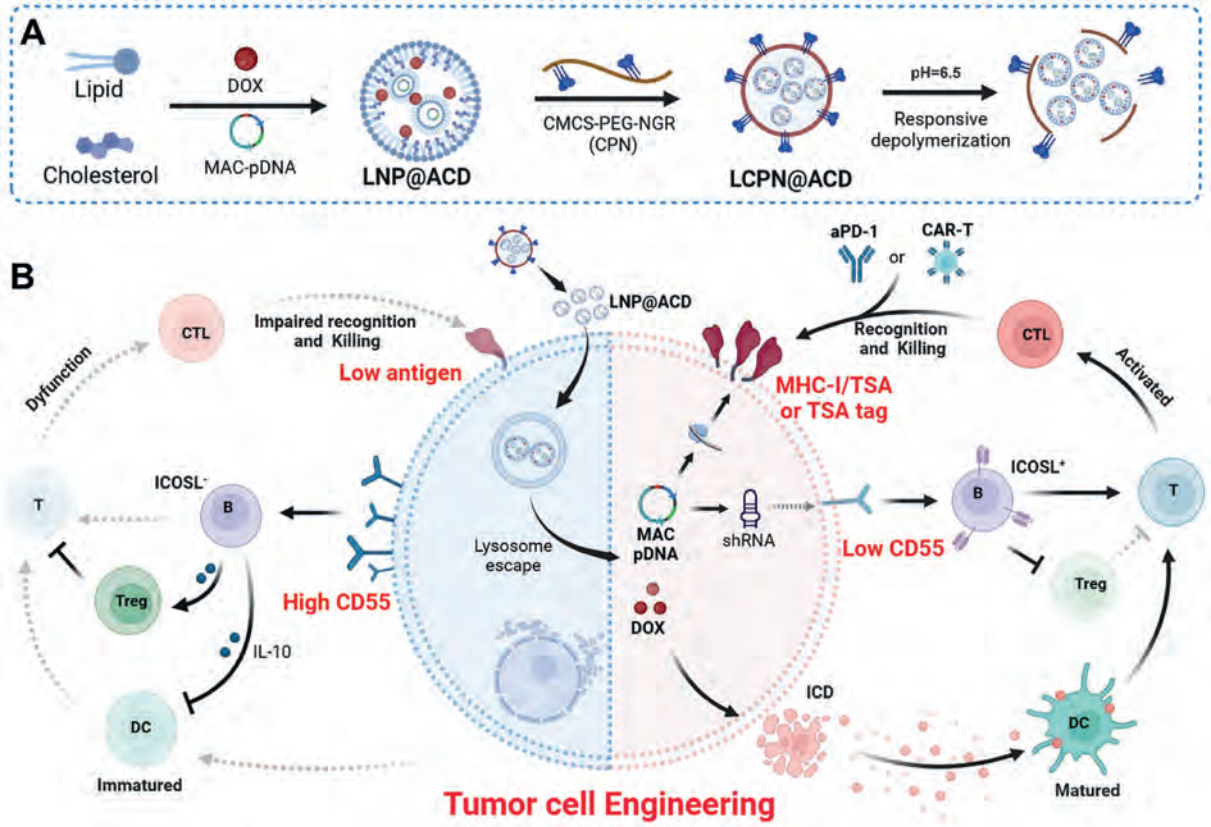

Figure 1 Schematic illustration of LCPN@ACD fabrication and tumor cells editing to improve the effect of immunotherapy. (A) LCPN@ACD is prepared as core−shell nanoparticles, targeting tumor tissue by NGR and disassembling in the acidic TME. (B) *In situ* tumor cell engineering strategy reversed immune escape by restore T-cell recognition and relieve immunosuppressive TME. LNP@ACD is readily initialized by tumor cells and releases MAC pDNA and DOX in the process of lysosome escape. MAC pDNA is translated to MCH-I/TSA, which is located on the surface of tumor cells, thus promoting the activation of the immune response and recognition of effector T cells. MAC pDNA is transcribed to CD55 shRNA to reduce tumor cell CD55 expression, which increases $ICOSL^+$ B-cell proportion and reverses the immunosuppressive microenvironment. DOX induces ICD and promotes DC maturation, further enhancing the antitumor immune response. The tumor dominated immune escape was reversed, which greatly enhanced the immunotherapeutic effect of aPD-1 and CAR-T therapies. This figure was created with BioRender.com.

were purchased from Beijing Biosynthesis Biotechnology Co., Ltd. (Beijing, China). Mouse HMGB1 ELISA Kit was purchased from Beijing Solarbio Science & Technology Co., Ltd. (Beijing, China). ELISA kits were purchased from Dakewe Biotech Co., Ltd. (Beijing, China). BioLegend (San Diego, USA) supplies all mouse antibodies for cytometry.

2.2. *Cell lines and animals*

Human umbilical vein endothelial cells (HUVEC) and Mouse colon cancer cells (MC-38) were obtained from Immocell (Xiamen, China) and cultured in RPMI 1640 cell culture medium containing 10% fetal bovine serum and 1% penicillin-streptomycin at 37 °C and 5% CO_2. C57BL/6 mice are bought from SPF Biotechnology Co., Ltd. All experimental procedures were executed according to the protocols approved by the Shandong University Animal Care and Use Committee (No. 19031).

2.3. *Preparation and characterization of LCPN@ACD*

Dlin-MC3-DMA, DSPC, DOTAP, cholesterol, and DOX (32:8:1:5:2) were dissolved in methanol/trichloromethane (1:5) solvent and desalted by adding three equivalents of triethylamine. The lipid-drug solution was transferred into a round bottom flask and evaporated under reduced pressure. The lipid film was hydrated with 1 mL of distilled water containing MAC pDNA for 30 min and sequentially passed through a 0.22 μm filter membrane and 100 and 50 nm liposome extruders to obtain LNP@ACD. LNP@ACD was added to an equal volume of CMCS-PEG_{2000}-NGR (2 mg/mL) under stirring to obtain LCPN@ACD.

2.4. *In vitro tumor microenvironment-sensitive charge and size dual response performance of LCPN@ACD*

One hundred microliters of LCPN@ACD was dispersed in 900 μL of PBS at different pH values. After incubation, the size and zeta potential were measured to verify its responsive depolymerization character in TME, and the experiment was repeated three times.

2.5. *Investigation of the in vitro release behavior of LCPN@ACD*

DOX solution was used as the control. One milliliter of DOX solution, LCPN@ACD, was placed in a dialysis bath to simulate

the release behavior in blood circulation. DOX was detected by using a UV spectrophotometer.

2.6. Active targeting and tumor accumulation study of LCPN@ACD

HUVECs were implanted on a 12-well plate for 12 h, and then the medium was refreshed with LNP@ACD-, LCPN@ACD-, and DOX (80 ng/mL)−containing medium. The CD13 endocytosis receptor on HUVECs was blocked by NGR for competitive inhibition experiments. HUVECs were imaged by inverted fluorescence microscopy. Cellular uptake of DOX in HUVECs was measured by C6 flow cytometry.

To evaluate the tumor accumulation ability, IR780 instead of DOX was selected to prepare LCPN. MC38 cells (1×10^6) were subcutaneously implanted. When the tumors grew to a suitable volume, 0.1 mL of IR780 solution, LNP@IR780, and LCPN@IR780 were injected intravenously. Then, the mice were anesthetized and visualized at time points. Twenty-four hours later, the main organs and tumors were collected and photographed.

2.7. Investigation of tumor microenvironment-sensitive cellular uptake behavior

In a 12-well disc, MC38 cells were inoculated overnight at a density of 1.0×10^5 cells/disc. Free DOX, LCPN@ACD (pH 7.4, 6.5), or LNP@ACD (80 ng/mL DOX) were supplemented. The nuclei were labeled with DAPI before imaging and flow cytometry assays.

2.8. Deep tumor penetration ability of LCPN@ACD

The MC38 cell suspension (20 μL/drop, dispersed in 0.24% methylcellulose medium) was incubated on the lid of the cell culture dish in an inverted position. Tumor spheres were bathed in a medium containing LNP@ACD and LCPN@ACD (pH 7.4 or 6.5) to allow DOX penetration. After 4 h of incubation, the tumor spheres were imaged by laser confocal microscopy.

2.9. Evaluation of lysosomal escape ability

The lysosomal escape of LCPN@ACD in MC38 cells was verified using AF488-DNA to replace MAC pDNA. First, MC38 cells were inoculated in confocal dishes (cell density 1.0×10^5 cells/well). After the cells were attached, 1 mL culture medium (pH = 6.5) containing 1 μg/mL AF488-DNA or LCPN@AF488-DNA was added and incubated for 2 or 5 h. The lysosomes were stained with LysoTracker red, and the nuclei were labeled with Hoechst 33342. The lysosomal escape ability of LCPN@ACD was visualized and analyzed with laser confocal microscopy.

2.10. In vitro cytotoxicity evaluation

MC38 cells (5×10^3) were seeded in each 96-well Plate 12 h before. Different preparations containing a series of DOX concentrations (0.0125, 0.05, 0.2, 0.8, and 3.2 μg/mL) were added. After 48 h of incubation, each well was treated with 20 μL of MTT (5 mg/mL) for 4 h. The supernatant was then replaced with DMSO for absorbance detection.

2.11. In vitro immunogenic cell death

MC38 cells were seeded at a density of 5×10^4 per well in 24-well discs. After incubation with saline, free DOX, LNP@ACD, and LCPN@ACD for 12 h (DOX concentration = 80 ng/mL), the cells were permeabilized (only for HMGB1 staining) and stained with CRT/HMGB1 antibody and AF488-conjugated secondary antibody, visualized under an inverted fluorescence microscope, and quantitatively analyzed by flow cytometry and ELISA. The secretion of ATP was determined with an ATP measurement kit.

2.12. Evaluation of transfection efficacy

MC38 cells (2×10^5) were seeded into each well. The experiments were grouped according to 1) naked MAC pDNA; 2) LNP@ACD; 3) LCPN@ACD (pH 7.4); and 4) LCPN@ACD (pH 6.5) (MAC pDNA = 1 μg/mL). Serum-free DMEM diluted formulations were incubated with MC38 cells for 8 h followed by complete medium replacement. After 48 h of transfection, the transfection efficiency was observed with fluorescence microscopy and quantified with flow cytometry.

A short peptide of OVA (SIINFEKL) was used to replace ASMTNMEL. After treating the cells as described above, the transfected and cell membrane-anchored MHC-I/SIINFEKL was labeled using an anti-mouse H-2Kb bound to SIINFEKL antibody. Anti-CD55 monoclonal antibody and AF594 secondary antibody were used for CD55 staining. Furthermore, the silencing efficacy of CD55 was detected through immunohistochemistry.

2.13. Preliminary study on the antitumor effect of LCPN@OCD

Four-to six-week-old C57BL/6 mice were used, with 1×10^6 cells injected subcutaneously. The groups were divided as follows: 1) saline, 2) free OVA pDNA, 3) LCPN@O, 4) LCPN@OD, 5) LCPN@OCD, and 6) LCPN@OCD + aPD-1. Formulations (2.5 mg/kg DOX and 2 mg/kg MOC pDNA) were intravenously administered every 3 days. Mice were sacrificed on the 14th day, and tissues were isolated for analysis. Three tumors from each group were excised to prepare a single-cell suspension for flow cytometry, and then 1000 μL of erythrocyte lysate was added to each tube to break up the erythrocytes. The $ICOSL^+$ B cells (stained with CD19-APC and CD275-PE) in the TME and OVA-specific CTLs (stained with SIINFEKL-H2Kb PE and CD8a-APC) in the spleen were determined by flow cytometry.

2.14. Enhanced antitumor effect of aPD-1 combined with LCPN@ACD

C57BL/6 mouse model subcutaneously carrying MC38 tumors (left side) was established. The groups were divided as follows: 1) saline; 2) blank LCPN; 3) DOX; 4) LCPN@D; 5) LCPN@AC; 6) LCPN@ACD; 7) LNP@ACD; 8) aPD-1; and 9) LCPN@ACD + PD-1mAb. Different formulations (2.5 mg/kg DOX, 2 mg/kg MOC pDNA, and 5 mg/kg PD-1 monoclonal antibody) were administered intravenously for 3 days. On Day 14, the model animals were killed, and the tumors were collected for weighing, photographing, and staining with H&E, Ki67, and TUNEL.

2.15. In vivo immune cell assay

Lymphocytes were extracted from the tumor and labeled with appropriate anti-mouse antibodies against DCs (CD11c, CD80, CD86), CTLs (CD3, CD8, IFN-γ), B cells (CD19 and CD275), and OVA-specific T cells (CD8 and SIINFEKL-H2Kb). Lymphocyte proportions were measured by flow cytometry.

2.16. Rechallenge study of LCPN@ACD in combination with aPD-1

Fourteen days after the first tumor incubation, 1×10^6 MC38 cells were implanted on the opposite side (right side). The mice were killed 28 days after the first tumor incubation. The tumors were collected, weighed, and photographed. T_{EM} cells (CD3, CD8, CD44, CD62L) in the spleen were detected to evaluate the immune memory effect of LCPN@ACD.

2.17. Antitumor effect study of LCPN@CCD combined with CAR-T cells

The MC38 tumor model was established as described previously. The mice were divided into 6 groups: 1) saline; 2) LCPN@D; 3) LCPN@CD; 4) LCPN@CCD; 5) CAR-T; and 6) LCPN@CCD + CAR-T. The formulations were administered at doses of 2.5 mg/kg DOX and 2 mg/kg MAC-pDNA. CAR-T cells were injected at 10^5 cells per mouse per injection. The animals were sacrificed on Day 14 and the tumors were separated, weighed, and photographed.

2.18. Rechallenge study of LCPN@CCD in combination with CAR-T cells

The experimental method was the same as in the "Rechallenge study of LCPN@ACD in combination with aPD-1" section.

2.19. Statistical analysis

All data are presented as the mean $\pm$ SD. The significance between two samples was analyzed by *t*-test and by one-way ANOVA in multiple samples. The significance and *P*-value were analyzed using GraphPad Prism8.0 software, $*P < 0.05$, $**P < 0.01$, and $***P < 0.001$.

3. Results and discussion

3.1. LCPN@ACD was successfully prepared with charge/size dual-conversion capacity

Specific binding of NGR and CD13 on tumor vascular endothelial cells, CMCS-PEG-NGR (CPN), was synthesized for active targeting. The NHS group of Mal-PEG_{2000}-NHS was attached to the amino group of carboxymethyl chitosan (CMCS) by the amide reaction, and then the maleimide end and the sulfhydryl end of the NGR peptide were reacted to finally produce CPN. The product was structurally confirmed by ^{1}H-NMR (Supporting Information Figs. S1 and S2). The characteristic peaks appeared in the product spectra, indicating the successful synthesis of CPN. Cationic lipid nanoparticles loaded with MAC pDNA (Supporting Information Fig. S3) and DOX (LNP@ACD) were prepared by a thin film dispersion method. To achieve responsive disintegration in TEM and enhance the accumulation in tumor tissues, LCPN@ACD was constructed by wrapping CPN around LNP@ACD using the electrostatic adsorption method. As shown in Fig. 2A, the particle size of LNP@ACD was 42.02 $\pm$ 2.17 nm, and the zeta potential was 18.81 $\pm$ 2.15 mV. As shown in Fig. 2B, the particle size of LCPN@ACD was 162.33 $\pm$ 9.59 nm, with a potential of -32.67 ± 1.75 mV, showing a sphere-like shape. The changes in size and zeta potential indicated that LNP@ACD was successfully wrapped by CPN. Information on the particle size, potential, and drug loading of LNP@ACD and LCPN@ACD is displayed in Supporting Information Tables S1 and S2. When LCPN@ACD reached the TME, LCPN@ACD was charged positively to decompose and release the small cationic liposomes LNP@ACD. As shown in Fig. 2C and D, the size of LCPN@ACD was 121.8 $\pm$ 7.12 nm at pH 7.4, while the particle size shifted to 41.43 $\pm$ 5.47 nm at pH 6.5. The zeta potential of LCPN@ACD was -32.67 ± 1.75 mV at pH 7.4, while the zeta potential flipped to 9.33 $\pm$ 1.94 mV at pH 6.5. In Fig. 2E, the cumulative DOX release from LCPN@ACD was 40.32 $\pm$ 1.53% at pH 7.4 for 48 h. The cumulative DOX release was higher at pH 6.5 (61.88 $\pm$ 1.53%, $P < 0.05$), indicating that LCPN@ACD could undergo responsive decomposition in the acidic TME, thus promoting DOX release. These results indicated that under a simulated acidic TME, the shell CPN of LCPN@ACD underwent protonation, and LCPN@ACD responsively depolymerized to expose the cationic core LNP@ACD, which could achieve a dual response transition in size and charge. LCPN@ACD was stable in PBS at 4 °C and in plasma at 37 °C (Fig. 2F and Supporting Information Fig. S4). More importantly, LCPN@ACD could well protect pMAC from degradation in a plasma condition (Supporting Information Fig. S5). In conclusion, the above results indicated that LCPN@ACD was successfully prepared and had good stability.

In addition, cellular uptake experiments (Fig. 2G–I) indicated that the fluorescence of LCPN@ACD was significantly stronger at pH 6.5 than at pH 7.4 ($P < 0.01$, $P < 0.001$), which was due to CPN-responsive shedding in the environment, exposing the cationic core of LNP@ACD and thus enhancing its uptake by tumor cells. These results showed that LCPN@ACD could undergo charge and size double conversion in the TME and enhance the uptake ability of tumor cells.

3.2. LCPN@ACD showed tumor tissue targeting, tumor penetration, and lysosomal escape capabilities

The targeting performance of LCPN@ACD was investigated by cell uptake assay and near-infrared fluorescence imaging. CD13-positive HUVECs were employed to validate the targeting effect of LCPN@ACD *in vitro*. The mean fluorescence intensity (MFI) of LCPN@ACD was significantly higher than that of LCP@ACD in HUVECs, which was corroborated by quantitative flow cytometric analysis ($P < 0.01$) (Fig. 3A–C). To verify NGR-mediated cellular uptake, HUVECs were pretreated using free NGR and then incubated using LCPN@ACD. The DOX fluorescence in LCPN@ACD was brighter than that in LCPN@ACD + free NGR ($P < 0.01$) because CD13 on HUVECs was saturated by free NGR, preventing it from interacting with NGR on LCPN@ACD. The higher cellular uptake efficiency of LCPN@ACD than that of LCP@ACD and NGR + LCPN@ACD groups suggests that NGR-mediated targeting can significantly improve cellular uptake efficiency and is expected to increase the accumulation of nanomedicines at the tumor site. In addition, NGR-mediated tumor

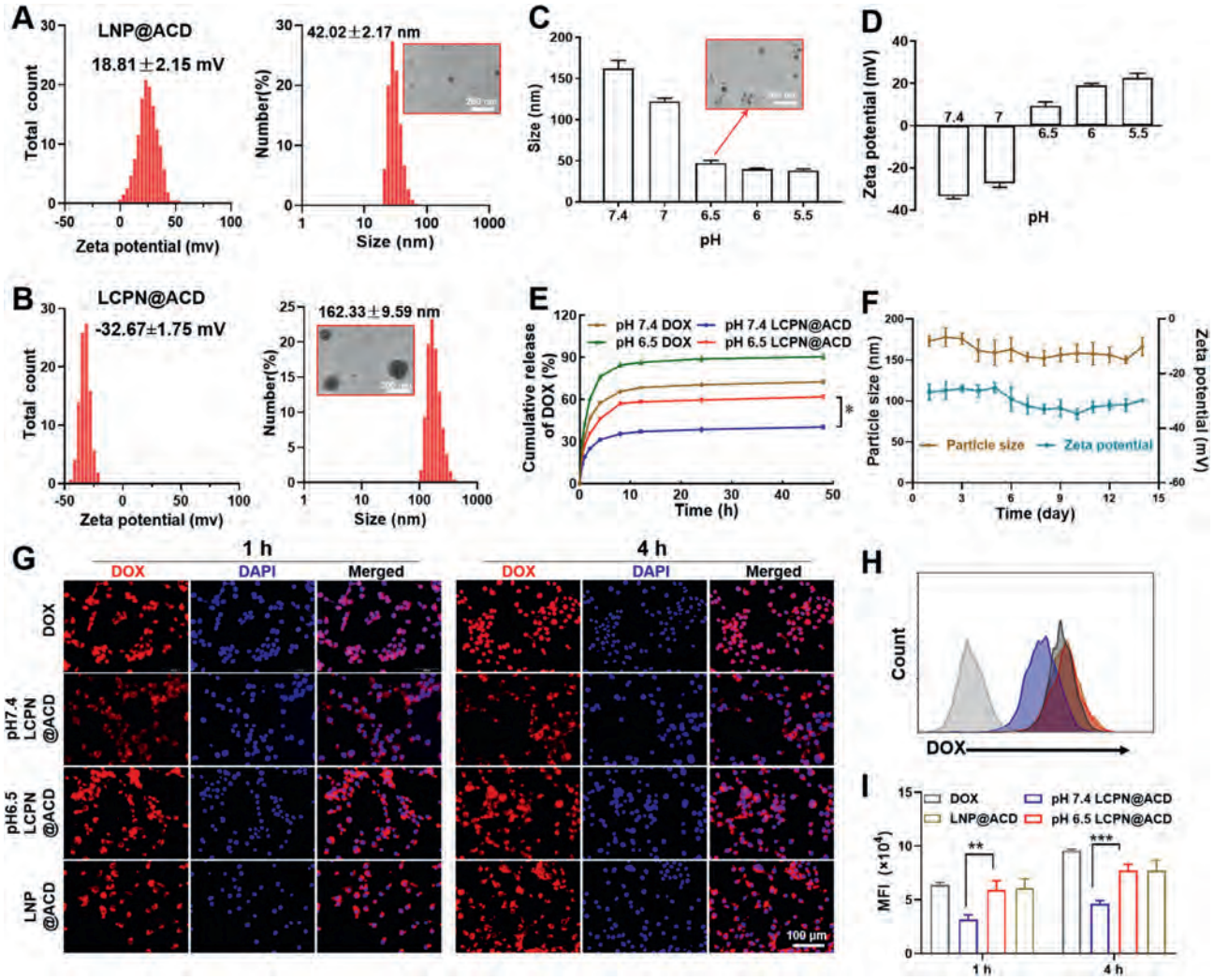

Figure 2 LCPN@ACD was successfully prepared with charge/size dual-conversion capacity. Zeta potential, particle size and morphology of LNP@ACD (A) and LCPN@ACD (B), scale bar = 200 nm. (C, D) Size and zeta potential of LCPN@ACD at different pH values. (E) Cumulative release curves of DOX at different pH condition within 48 h. (F) The particle size and zeta potential stability of LCPN@ACD at 4 °C for 14 days. (G) Cellular uptake of LCPN@D on MC38 cells at different pH condition, scale bar = 100 μm. Representative flow diagram (H) and fluorescent intensity (I) of MC38 cells ($n = 3$). Data are presented as mean ± SD. *$P < 0.05$, **$P < 0.01$ and ***$P < 0.001$.

accumulation capacity was investigated in MC38-bearing C57BL/6 mice using near-infrared fluorescence imaging. IR780 was utilized to replace DOX and prepare LCP@ACI and LCPN@ACI. As shown in Fig. 3D, the tumor sites treated with LCPN@ACI showed a higher MFI than the IR780 and LCP@ACI (without NGR) groups. *Ex vivo* imaging (Fig. 3E and F) also demonstrated that LCPN@ACI significantly increased the distribution in the tumor, indicating NGR-mediated tumor targeting. Taken together, the above results indicated that LCPN@ACI could achieve active targeting of tumor tissue mediated by NGR.

Once the drug delivery system reaches the tumor site, it needs to penetrate into the tumor tissue. However, it is difficult for carriers to penetrate deeply into dense tumor tissue. It has been shown that positively charged and small nanoparticles have stronger tumor penetration ability[29-30]. LCPN@ACD, as a charge-particle size reversible system, could achieve size and charge dual reversal at pH 6.5 to release positively charged and small LNP@ACD. To demonstrate that the charge and size dual conversion property of LCPN@ACD could enable deep penetration in tumors, we investigated the deep tumor penetration of LCPN@ACD in tumorspheres. As shown in Fig. 3G and H, significant differences in fluorescence intensity were observed between the LNP@ACD, LCPN@ACD (pH = 7.4), and LCPN@ACD (pH = 6.5) groups at 100 and 120 μm deep of the tumor spheres. Among them, the fluorescence intensity of the LCPN@ACD (pH = 6.5) and LNP@ACD groups was significantly stronger than the LCPN@ACD group, which indicated a stronger deep penetration ability of LCPN@ACD (pH = 6.5) and LNP@ACD groups. The enhanced deep penetration of LCPN@ACD is attributed to the release of LNP@ACD in the acidic microenvironment and the small particle size and positive charge of LNP@ACD.

pDNA degradation in lysosomes severely inhibited the expression efficiency. Therefore, the lysosomal escape ability of LCPN@ACD was investigated by confocal microscopy. The intracellular fate of the plasmid was investigated by replacing the

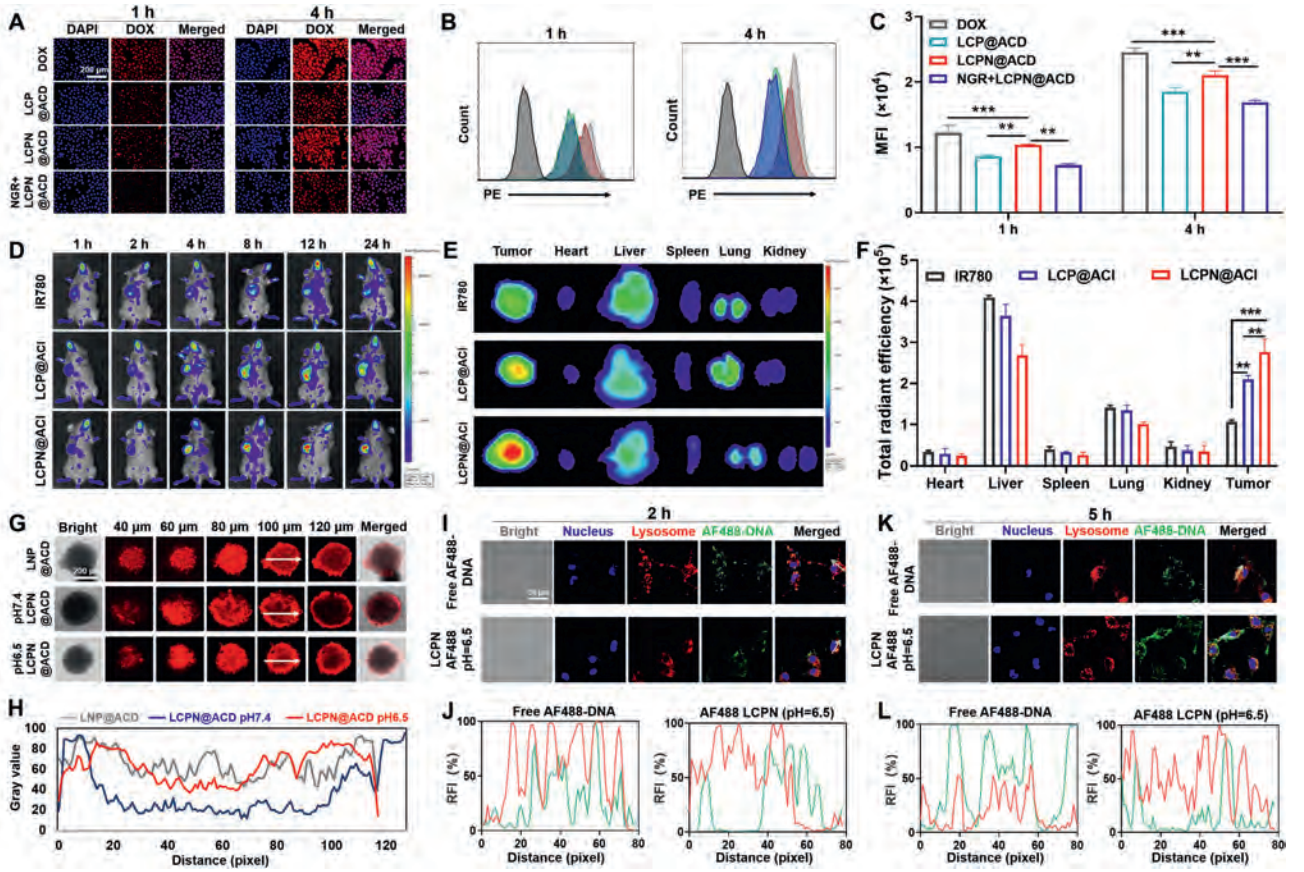

Figure 3 LCPN@ACD showed tumor targeting, tumor penetration and lysosomal escape capabilities. Representative images (A), flow diagram (B) and quantified data (C) of cellular uptake on HUVECs, scale bar = 200 μm. Fluorescent images of mice administered with IR780-containing formulations (D). The *ex vivo* imaging (E) and total fluorescence intensity (F) of major organs 24 h after IR780-containg formulations administrated intravenously. (G) Images of MC38 tumor spheroids after incubation with DOX-containing formulations for 5 h, scale bar = 200 μm. (H) Quantified fluorescence intensity of tumor sphere slices. Representative image and fluorescence distribution of AF488-pDNA and lysosome in MC38 cells after incubated with AF488-pDNA and LCPN-AF488 (pH = 6.5) for 2 h (I and J) and 5 h (K and L), scale bar = 30 μm. Lysosome was labeled in red, AF488-pDNA was in green. Line in red represent the fluorescent intensity of lysosome, line in green represent the fluorescent intensity of AF488-pDNA. LNP@ACD represents drug loaded inner lipid nanoparticle; LCP@ACD represents CMCS-PEG modified LNP@ACD; LCPN@ACD represents CMCS-PEG-NGR modified LNP@ACD; LCPN@ACI represents LCPN@ACD after the replacement of DOX by IR780. Data are presented as mean ± SD (n = 3). *$P < 0.05$, **$P < 0.01$ and ***$P < 0.001$.

MAC pDNA with AF488-DNA (green fluorescence). In Fig. 3I and J, after 2 h of incubation with MC38 cells, LCPN AF488-pDNA (pH = 6.5) showed less overlap between AF488-pDNA and lysosomes, greater AF488-pDNA distribution in the cytoplasm, when compared with free AF488-pDNA group. At the time point of 5 h, the green fluorescence of AF488-pDNA in the free group overlapped mostly with the lysosome, while the green fluorescence of LCPN AF488-pDNA (pH = 6.5) overlapped less with the red fluorescence of the lysosomes (Fig. 3K and L). The Pearson's *R*-value of LCPN AF488 (pH = 6.5) was lower than that of AF488-pDNA at both 2 and 5 h, and the difference in Pearson's *R*-value between the two groups was further increased at 5 h (Pearson's *R*-value of AF488-pDNA at 2 h was 0.88; Pearson's-*R* value of LCPN AF488 (pH = 6.5) at 2 h was 0.72. Pearson's R-value of AF488-pDNA at 5 h was 0.89; Pearson's-*R* value of LCPN AF488 (pH = 6.5) at 5 h was 0.63), which indicates that LCPN AF488 (pH = 6.5) has lower overlap with lysosomes compared to AF488-pDNA, *i.e.*, LCPN AF488 (pH = 6.5) has stronger lysosomal escape ability (Supporting Information Fig. S6). The above results suggested that LCPN@ACD could promote the escape of the plasmid from lysosomes to the cytoplasm, which could prevent its degradation by lysosomes.

3.3. LCPN@ACD edited tumor cells to be featured in high MHC-I/TSA expression, low CD55 expression, and immunogenetic cell death

T-cell recognition and killing of tumors is severely limited by low levels of antigen expression. Here, we hypothesized that T-cell recognition and killing could be restored by artificially upregulating MHC-I/TSA expression. The working mechanism of LCPN@ACD *in vivo* and *in vitro* was verified. First, the transfection efficiency of LCPN@ACD was investigated, and fluorescence images and flow cytometry quantification of MC38 tumor cells *in vitro* showed that higher transfection efficiency was reached in the LNP@AC and LCPN@AC (pH 6.5) groups (Fig. 4A−C). In Supporting Information Fig. S7, the Western blot result verified the overexpression of MHC-I on MC38 cells. The *in vivo results* showed that LCPN@ACD exhibited higher

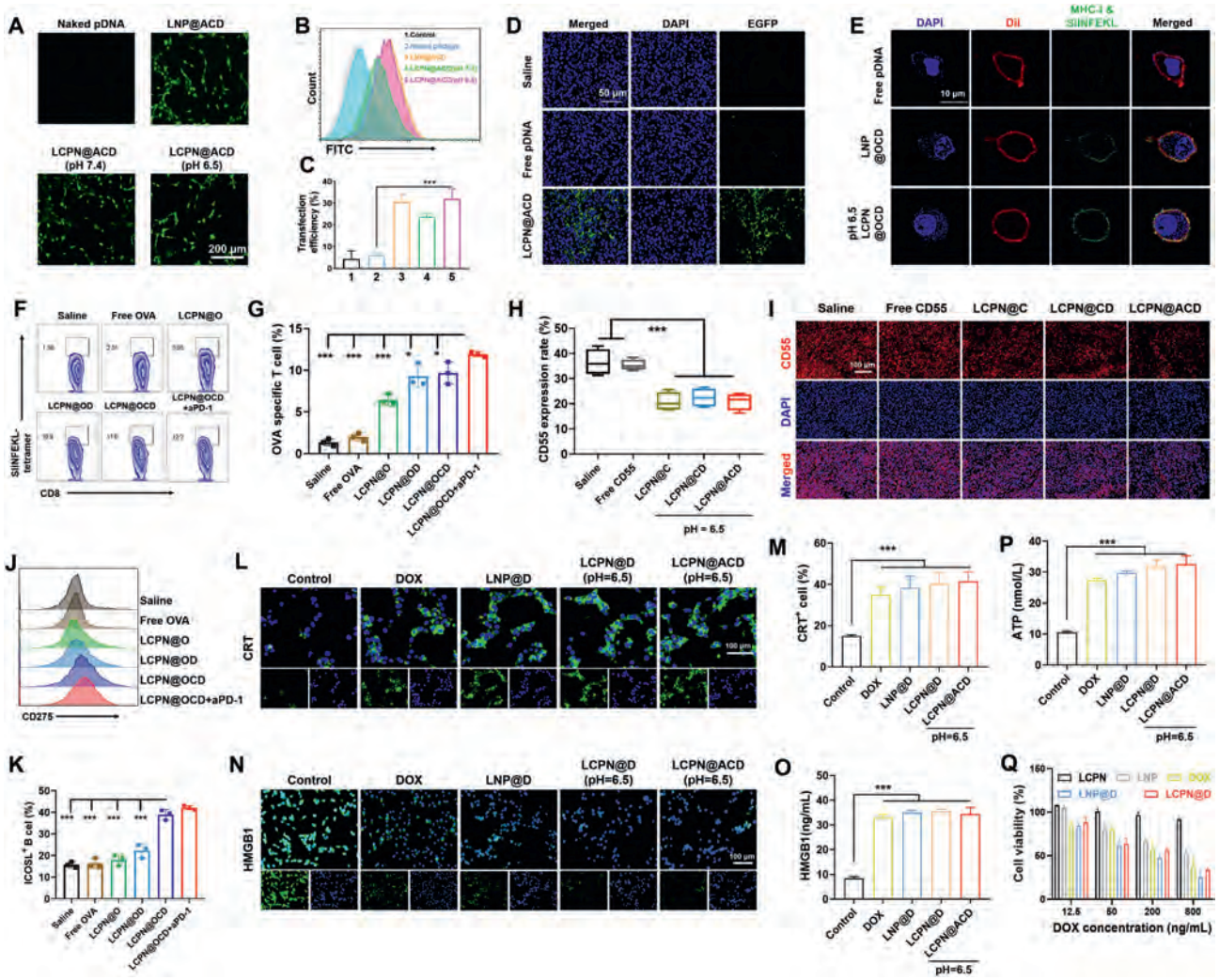

Figure 4 LCPN@ACD upregulate tumor MHC-I/TSA, downregulate tumor CD55 and induce ICD effect. Fluorescence microscope images (A), flow diagram (B) and fluorescent intensity (C) of MC38 cells 48 h after incubated with LCPN@ACD *in vitro* ($n = 3$), scale bar = 200 μm. (D) Tumor slice analysis of EGFP expression at the tumor site. Scale bar = 50 μm. (E) Confocal microscopy image of MHC-I/SIINFEKL expression on MC38 cells, scale bar = 10 μm. (F, G) Flow cytometry of OVA-specific T cells in spleens ($n = 3$) after the administration of LCPN@OCD. (H) *In vitro* flow cytometry analysis of CD55 expression after incubated with LCPN@ACD ($n = 3$). (I) Immunofluorescence staining of CD55 in tumor tissues after administration of LCPN@ACD, scale bar = 100 μm. (J, K) Flow cytometry analysis of $ICOSL^+$ B cells in tumor tissue after administration of LCPN@OCD ($n = 3$). Fluorescence microscope images (L) and quantitative analysis (M) of CRT exposure tumor cells and HMGB1 released tumor cells (N and O) after treated with DOX-containing formulations, scale bar = 100 μm. ELISA analysis of ATP (P) released from MC38 cells. (Q) *In vitro* cell viability of MC38 cells treated with different formulations ($n = 3$). The O in LCPN@OCD expressed OVA, and the A in LCPN@ACD expressed ADPGK. Data are presented as mean ± SD. $^*P < 0.05$, $^{**}P < 0.01$ and $^{***}P < 0.001$.

transfection efficiency in the tumor tissues of MC38-bearing mice (Fig. 4D). In conclusion, these results suggested that LCPN@ACD could achieve effective transfection of tumor cells.

Increasing the expression level of MHC-I in tumors is an important means to improve antitumor immunity[12,14]. However, the lack of tumor antigens (especially TSA) is an important problem facing immunotherapy at present. Therefore, this study integrated the genes of MHC-I and ASMTNMELM into one plasmid. The plasmid simultaneously translated MHC-I and ASMTNMELM, which rapidly bound to the MHC-I/ASMTNMELM complex without further processing and then transferred onto the tumor cell surface. The MHC−I binding peptide (SIINFEKL) of ovalbumin (OVA) was used to prepare LCPN@OCD, which was applied to substitute ASMTNMELM, thus evaluating antigen-specific T cells. In Fig. 4E, the LCPN@OCD and LNP@OCD groups had significantly higher fluorescence intensity than the free pDNA group, indicating that LCPN@OCD could effectively express MHC-I/OVA on tumor cells. Moreover, mice were immunized with OVA-specific antigen peptides after replacing ASMTNMELM to investigate the infiltration of antigen-specific T-cell responses. OVA-specific T cells were tested in spleens isolated from the mice (Fig. 4F and G). No significant increase was shown in OVA-specific T cells in the saline, free OVA-treated group, while the ratio of OVA-specific T cells was increased to different degrees in the LCPN@O, LCPN@OD, LCPN@OCD and LCPN@OCD + aPD-1 groups,

with the highest in the LCPN@OCD + aPD-1 group, which was 6 times higher than that in the Free-OVA group, indicating that LCPN@OCD could induce the production of antigen-specific $CD8^+$ T in the body more effectively. These results confirmed that LCPN@OCD could induce tumor MHC-I/OVA expression to boost the generation of $CD8^+$ T cells.

B cells are important components in the TME[24]. Previously, we slightly alleviated the immunosuppressive TME by a B-cell depletion strategy; however, B-cell subtypes play different roles in antitumor immunity, and targeted regulation of specific B-cell subtypes may overcome the deficiency of whole B-cell depletion to promote antitumor immunity. Effective inhibition of CD55 protein is essential to achieve B-cell subtype conversion after DOX-induced chemotherapeutic effects. As shown in Fig. 4H, I and Fig. S7, after incubation with different groups, the groups containing the CD55-interfering gene (LCPN@C, LCPN@CD and LCPN@ACD) exhibited weaker fluorescence intensity, and CD55 expression in the saline group was 1.8 times greater than that in the LCPN@ACD group ($P < 0.001$), demonstrating that LCPN@ACD could effectively interfere with CD55 expression. Next, we further explored the expression kinetics of LCPN@ACD. CD55 and MHC-I expression were detected over 3 generations after MC38 cells were administrated with LCPN@ACD (Supporting Information Fig. S8). It can be implied that LCPN@ACD maintains expression no more than 3 generations, and the mouse should better be administrated within 3 days between each time. Analysis of intra-tumoral B cells (Fig. 4J and K) showed that the group containing the CD55-interfering gene had more $ICOSL^+$ B cells than the group without the CD55-interfering gene. In summary, LCPN@ACD efficiently inhibited the expression of CD55 to promote the generation of $ICOSL^+$ B cells.

Antigen presentation and activation of T cells by DCs is a key factor affecting the antitumor efficacy of T cells[31,32]. Enhancement of DC infiltration and maturation in tumor tissue, such as ICD, is necessary to trigger antitumor immunity. DOX can induce ICD effects after being taken up into tumor cells. Fluorescence microscopy (Fig. 4L) and quantitative analysis (Fig. 4M) indicated that the CRT-positive rate was increased after incubation with free DOX, LNP@D, and LCPN@D ($P < 0.001$). Investigation of HMGB1 release demonstrated that free DOX, LNP@D, and LCPN@D could induce more HMGB1 release than the control, *i.e.*, more HMGB1 was present in the culture medium (Fig. 4N) and less HMGB1 in tumor cells (Fig. 4O). By assessing ATP secretion, we found that incubation with free DOX, LNP@D, and LCPN@D significantly induced more ATP secretion ($P < 0.001$, Fig. 4P). The results demonstrated that the groups containing DOX (including LCPN@D) could effectively induce ICD. Moreover, LCPN@ACD shows the same ICD induction ability as LCPN@D, which implies that the presence of MAC pDNA does not affect the ICD induction ability of LCPN@D. As a traditional chemotherapeutic agent, DOX can kill tumor cells in tumor tissues, reduce tumor density, and enhance immune cell infiltration[33,34]. The cytotoxicity of LCPN@OCD was investigated. In Fig. 4Q, blank LCPN had no significant cytotoxicity in the set concentration range, and the nanoparticles had a better safety profile. Although the cytotoxicity of DOX, LNP@D, and LCPN@D was concentration-dependent, tumor cells maintained good cell viability at the DOX concentration (80 ng/mL) used in this study to induce tumor ICD, which made a guarantee for the efficiency of pMAC drug.

3.4. LCPN@OCD enhances aPD-1 effect and activated antitumor immune response

A preliminary evaluation of the efficacy of LCPN@OCD was performed in MC38 tumor-bearing mice. Fig. 5A and B showed the schedule of administration and group setting. In Fig. 5C, tumor growth in the LCPN@OCD and LCPN@OCD + aPD-1 groups were obviously inhibited, and tumor growth was slowest in the LCPN@OCD + aPD-1 group. Tumor weights, tumor photo and tumor inhibition rate (Fig. 5D, Supporting Information Fig. S9 and Table S3) also showed that the LCPN@OCD group and the LCPN@OCD + aPD-1 group had excellent antitumor effects, and the LCPN@OCD + aPD-1 group had the best antitumor effect. In Fig. 5E, no significant difference was shown in mouse weight, indicating that the formulations had less systemic toxicity. In brief, LCPN@OCD had an excellent antitumor effect, which was further enhanced with the addition of aPD-1. Several key immune cells in the TME were assayed for a preliminary evaluation of the immunomodulatory function of LCPN@OCD. As shown in Fig. 5F and G, both the LCPN@OCD and LCPN@OCD + aPD-1 groups significantly promoted DC maturation, with the highest percentage of mature DCs measured in the LCPN@OCD + aPD-1 group ($P < 0.001$). In Fig. 5H and I, the proportions of $CD8^+$ T cells and $CD4^+$ T cells in the LCPN@OCD + aPD-1 group were the highest at 20.8 ± 3.08% and 30.73 ± 2.31%, respectively. These results preliminarily confirmed that LCPN@OCD had a regulatory effect on the tumor immune microenvironment and a boosting effect on aPD-1. The above results verified that LCPN@OCD could achieve tumor MHC-I/OVA expression to promote $CD8^+$ T-cell function, inhibit the expression of CD55 to boost the generation of $ICOSL^+$ B cells, have an excellent ICD effect, and effectively inhibit the development of tumor cells. Furthermore, in a preliminary antitumor effect study, LCPN@OCD showed excellent antitumor effects and immune cell regulatory functions and enhanced the therapeutic effect of aPD-1.

3.5. LCPN@ACD leads to excellent antitumor effects and enhanced aPD-1 effect

LCPN@ACD *in vivo* antitumor assays were performed on MC38 tumor-bearing mice. The administration profile and group setting are shown in Fig. 6A and B. Compared with the other groups, tumor growth was slower in the LCPN@ACD group and LCPN@ACD + aPD-1 group, the slowest tumor growth rate was observed in the LCPN@ACD + aPD-1 group ($P < 0.001$, compared with LCPN@ACD) (Fig. 6C and Supporting Information Fig. S10), indicating that LCPN@ACD had an excellent antitumor effect and further improved the antitumor effect after combination with aPD-1. Tumor weights and tumor photos also showed (Fig. 6D and Fig. S10) that the LCPN@ACD group and the LCPN@ACD + aPD-1 group had excellent antitumor effects compared with the other groups, and the antitumor effect of the LCPN@ACD + aPD-1 group was better. To detect the effect of LCPN@ACD and its enhancement on aPD-1, an immunohistochemical experiment of tumor tissue was performed, as shown in Fig. 6E. The necrotic area of tumor cells in the LCPN@ACD + aPD-1 group was the largest, and the necrotic area of tumor cells by H&E staining in the LCPN@ACD and LCPN@ACD + aPD-1 groups was significantly higher than that in the other groups. Ki67 in brown−yellow positive cells (proliferating cells) were significantly decreased in both the

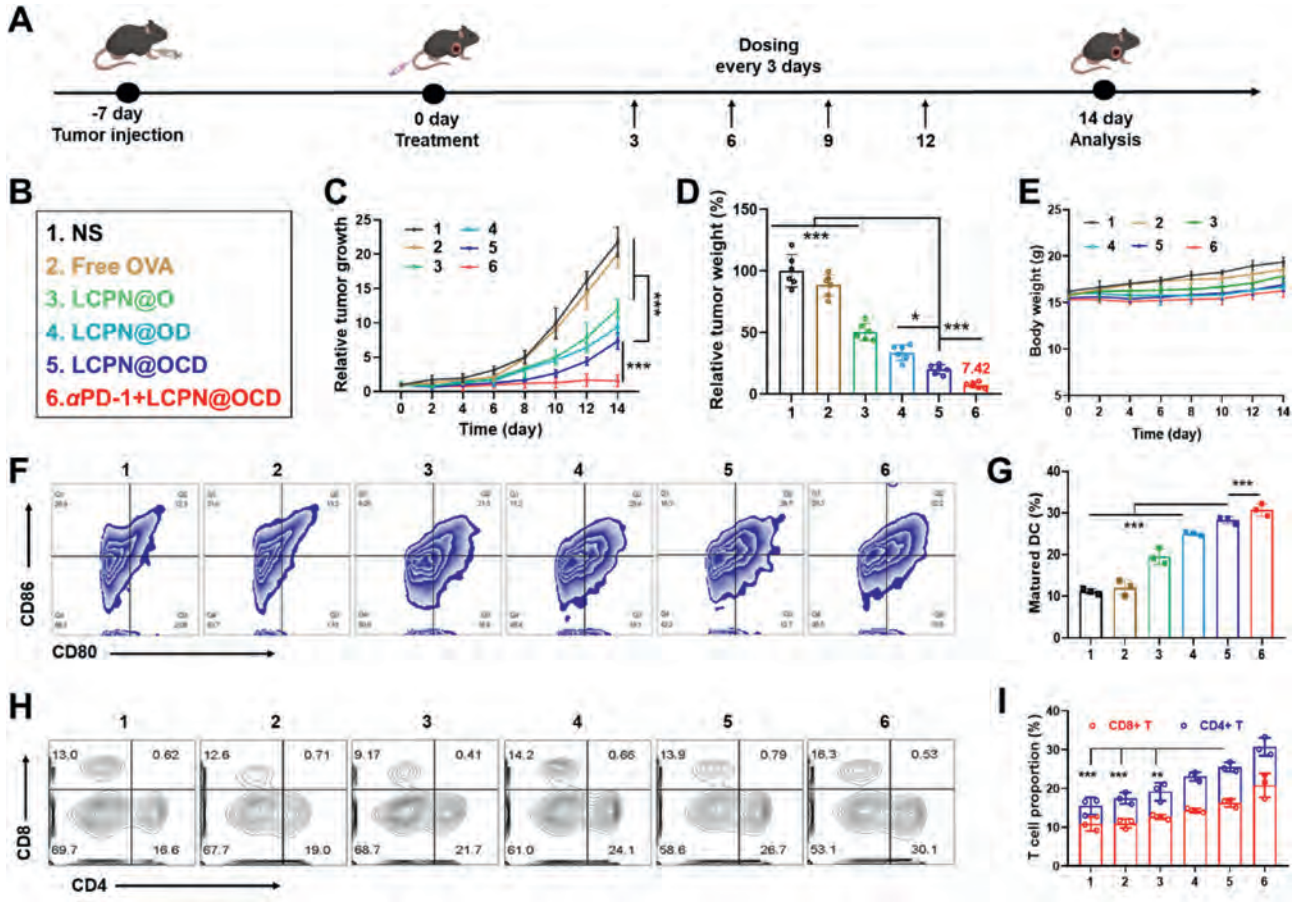

Figure 5 Preliminary antitumor effect and immune stimulation ability of LCPN@OCD. (A) Schedule of administration. (B) Groups of the antitumor experiment for Fig. 5C-I. (C) Tumor growth curves in different formulation-treated mice ($n = 6$). (D) The tumor weights on Day 14 ($n = 6$). (E) Body weights recorded every 2 days within 14 days ($n = 6$). (F, G) Flow cytometry analysis of mature DCs in tumors ($n = 3$). (H, I) Flow cytometric analysis of $CD4^+$ and $CD8^+$ T cells in tumors ($n = 3$). Data are presented as mean ± SD. $^*P < 0.05$, $^{**}P < 0.01$ and $^{***}P < 0.001$.

LCPN@ACD group and the LCPN@ACD + aPD-1 group, and the brown-yellow positive cells in the LCPN@ACD + aPD-1 group were the least, which indicated that the LCPN@ACD + aPD-1 group had the strongest inhibitory effect on tumors. TUNEL assays showed that tumor cell apoptosis was obviously increased in the LCPN@ACD and LCPN@ACD + aPD-1 groups (green fluorescence), and the LCPN@ACD + aPD-1 group had the most apoptosis, which indicated that the LCPN@ACD + aPD-1 group had the highest apoptosis rate. Taken together, these results indicated that LCPN@ACD had a great antitumor effect and could strengthen the therapeutic effect of aPD-1.

Furthermore, the long-term antitumor effect was evaluated through a rechallenge experiment. As shown in Fig. 6F and G and Supporting Information Fig. S11, tumor growth after the rechallenge experiment was inhibited in the LCPN@ACD and LCPN@ACD + aPD-1 groups compared with the control group ($P < 0.001$). Furthermore, after the rechallenge study, the $CD4^+$ T_{EM} and $CD8^+$ T_{EM} percentages in the LCPN@ACD group and the LCPN@ACD + aPD-1 group were greater than those in the control group ($P < 0.001$), confirming long-term immune memory in the LCPN@ACD and LCPN@ACD + aPD-1 treatment groups (Fig. 6H−K). Together, these results demonstrated that mice treated with LCPN@ACD or LCPN@ACD + aPD-1 have long-term antitumor effects.

In addition, the safety of LCPN@ACD was preliminarily evaluated through a hemolysis test and histopathological analysis of the major organs. The weight changes of mice during treatment (Supporting Information Fig. S12) also suggested that LCPN@ACD had some systemic safety. In Supporting Information Fig. S13, no significant tissue damage was observed, indicating that LCPN@ACD was safe for major organs. The safety of injection was investigated by a hemolysis experiment (Supporting Information Fig. S14), and the results showed no obvious hemolysis phenomenon in the experimental concentration range (5−80 μg/mL), and the hemolysis rate was less than 5%. The hemolysis results demonstrated that LCPN@ACD had less interaction with erythrocytes and was suitable for intravenous injection. Overall, these results indicated that LCPN@ACD had excellent biocompatibility and safety.

3.6. LCPN@ACD could effectively reverse the TIME and further enhance the antitumor immune responses

The TIME remodeling effect of LCPN@ACD was investigated by measuring the number of immune cells and the level of cytokines,

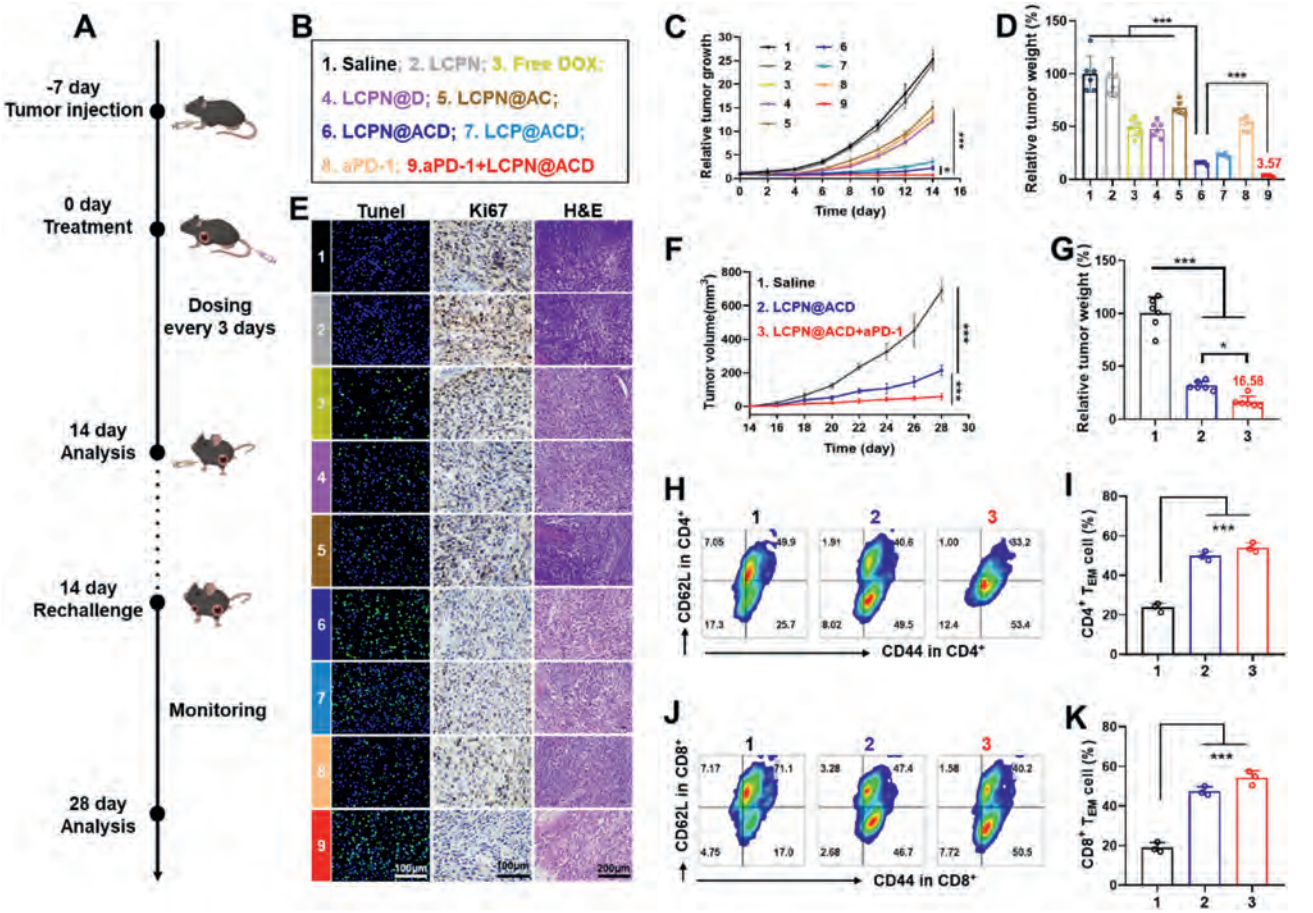

Figure 6 LCPN@ACD showed excellent antitumor effects and enhanced the therapeutic effect of aPD-1 in a subcutaneous tumor model and rechallenge study. (A) Schedule of treatments on MC38 tumor-bearing mice. (B) Groups setting for Fig. 6B−E. (C) Tumor growth curves within 14 days ($n = 6$). (D) Tumor weights on day 14 were recorded ($n = 6$). (E) H&E, Ki67 and TUNEL staining of tumor slices, scale bar = 100 or 200 μm. (F) Tumor volume changes in the rechallenged tumors ($n = 6$). (G) Tumor weight in different groups after the rechallenge study ($n = 6$). (H, I) Flow chart and quantitative analysis of $CD4^+$ $T_{EM\ cells}$ proportion in spleen on Day 28 ($n = 3$). (J, K) Flow chart and quantitative analysis of $CD8^+$ $T_{EM\ cells}$ proportion in spleen on Day 28 ($n = 3$). The group setting for Fig. 6G-K are consistent with Fig. 6F. Data are presented as mean ± SD. $^*P < 0.05$, $^{**}P < 0.01$ and $^{***}P < 0.001$.

groups were set as Fig. 7A. As shown in Fig. 7B and C, $ICOSL^+$ B cells in LCPN@ACD and LCPN@ACD + aPD-1 had higher positive rates than the others. Notably, $ICOSL^+$ B cells in the LCPN@ACD group were significantly higher than those in the LCPN@AC and LCPN@D groups ($P < 0.001$) due to the combination of chemotherapy induction and CD55 inhibition. In Fig. 7D and E, the proportion of DC maturation was increased in the treatment groups containing DOX, which could be attributed to the ICD effect of DOX. LCPN@ACD and LCPN@ACD + aPD-1 maximized the T-cell proportion in the TIME (*vs.* saline, $P < 0.001$) (Fig. 7F and G), indicating that LCPN@ACD could effectively promote the intratumor invasion of lymphocytes. CTLs were evaluated in Fig. 7H and I. In comparison with the others, the proportion of CTLs was higher in the LCPN@ACD and LCPN@ACD + aPD-1 groups, indicating that LCPN@ACD could enhance the tumor infiltration of CTLs. In addition, the LCPN@ACD group and the LCPN@ACD + aPD-1 group had lower levels of Tregs and higher $CD8^+$ T-cell/Treg ratios than the other groups (Fig. 7J−L). For the determination of immune cytokines (Fig. 7M and Supporting Information Fig. S15), the LCPN@ACD group and the LCPN@ACD + aPD-1 group induced more immune-activating cytokines (IL-6, IFN-γ, and IL-12) and less immunosuppressive cytokines (TGF-β and IL-10). In summary, LCPN@ACD could effectively reverse the TIME, which would benefit aPD-1 therapy.

3.7. LCPN@CCD restores T cell recognition and enhances the effect of CAR-T therapy in a low antigen-expressing tumor model

Low expression or heterogeneity of tumor antigens leading to difficulties in finding suitable targets and insufficient tumor recognition are the key factors limiting CAR-T therapy for solid tumors[15]. Exogenous expression of specific antigens can overcome the problems of low antigen expression and heterogeneity and improve the efficacy of CAR-T therapy. On the other hand, an ameliorated tumor microenvironment can further contribute to CAR-T-cell therapy.

CEA is highly expressed in human colorectal cancer patients and has become an important target of tumor CAR-T therapy[1,8]. To simulate the heterogeneous population with low levels of tumor antigen, we chose mouse MC38 cells that do not express CEA as a

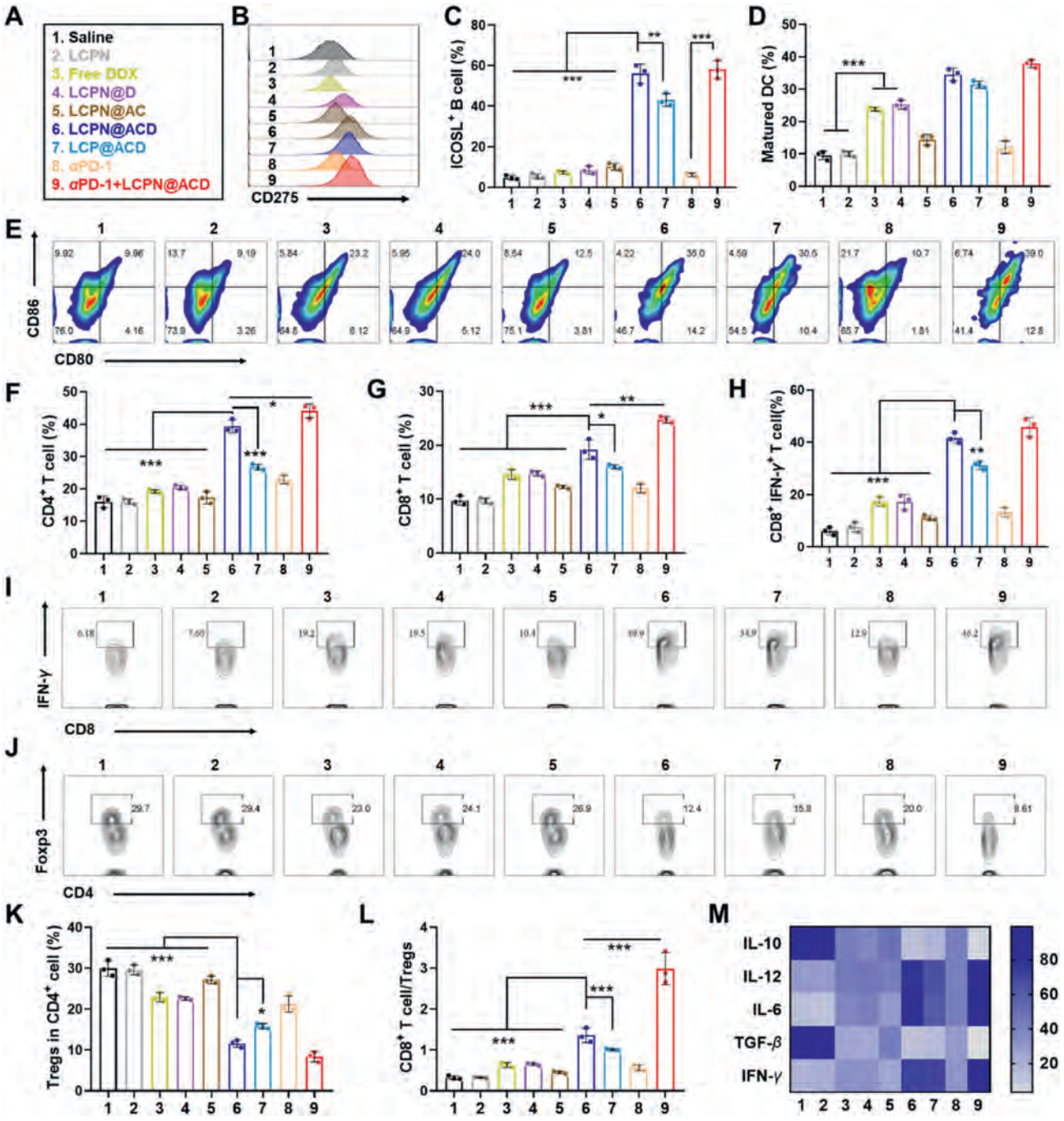

Figure 7 LCPN@ACD successfully reversed the TIME and further enhanced the immune response. (A) Groups. (B, C) Flow cytometry analysis of ICOSL$^+$ B cells in tumors ($n = 3$). (D, E) Analysis of mature DCs in tumors ($n = 3$). (F, G) Flow cytometry analysis of CD4$^+$ T cells and CD8$^+$ T cells ($n = 3$). (H, I) Analysis of tumor-infiltrating CTLs ($n = 3$). (J, K) Analysis of tumor-infiltrating Treg cells ($n = 3$). (L) Quantitative analysis of CD8$^+$ T/Tregs. (M) Heatmap of relative cytokine content in the TIME ($n = 3$). Data are presented as mean ± SD. *$P < 0.05$, **$P < 0.01$ and ***$P < 0.001$.

model for subsequent studies. MHC-I is not required in the process of CAR-T killing tumor cells, and we constructed a plasmid encoding both CEA-GPI and CD55 (CGC pDNA) and prepared LCPN@CCD. We exploited CEA CAR-T cells in MC38-bearing mice to verify the combination effect of LCPN@CCD and CAR-T-cell therapy. Fig. 8A shows a schematic diagram of the dosing schedule, which was administered every 3 days. In Fig. 8B and C and Supporting Information Fig. S16, the tumor growth curves, tumor weights, and tumor photo demonstrated that the antitumor effect of the LCPN@CCD + CAR-T group was better than that of the LCPN@CCD ($P < 0.01$) and CAR-T groups ($P < 0.001$), indicating that the combination could boost the antitumor effect. During administration, the weight of the mice was measured every two days. In Fig. 8D, no significant change in body weight was shown between groups, indicating that the combination of LCPN@CCD with CAR-T cells did not increase

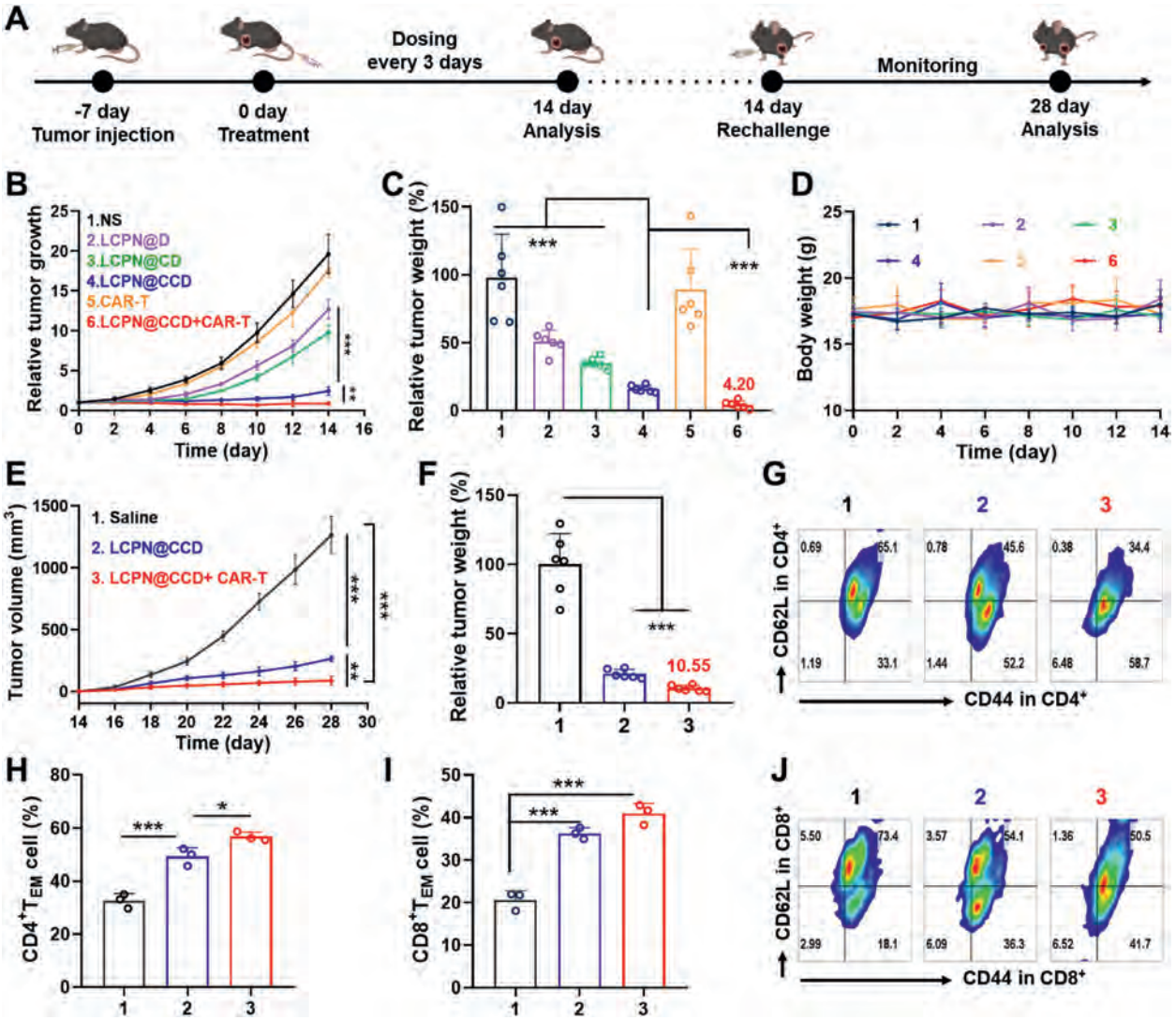

Figure 8 LCPN@CCD boosts the therapeutic effect of CAR-T cells on low antigen-expressing tumors. (A) Schematic illustration of administration schedule. Tumor growth curves (B) and tumor weights (C) of mice during administration ($n = 6$). (D) Body weights of mice ($n = 6$). (E) Tumor volume curves of rechallenged tumors ($n = 6$). (F) Tumor weights of rechallenged tumors ($n = 6$). (G, H) Proportion of $CD4^+$ T_{EM} cells in the spleen after the rechallenge study ($n = 3$). (I, J) Proportion of $CD8^+$ T_{EM} cells in the spleen after the rechallenge study ($n = 3$). Data are presented as mean ± SD. $^*P < 0.05$, $^{**}P < 0.01$ and $^{***}P < 0.001$. Fig. 8B contains the group setting for Fig. 8B–D; Fig. 8E contains the group setting for Fig. 8E–J.

systemic toxicity. These results suggested that LCPN@CCD could be combined with CAR-T to enhance its immunotherapy effect.

Furthermore, the long-term antitumor effect was evaluated, as shown in Fig. 8E–J. In Fig. 8E, it could be observed that rechallenged tumor growth was significantly inhibited with LCPN@CCD and LCPN@CCD + CAR-T ($P < 0.001$). Weighing and photos of the tumors after the rechallenge also confirmed this result (Fig. 8F and Supporting Information Fig. S17). After the rechallenge experiment, we found that the proportion of $CD4^+$ T_{EM} (Fig. 8G and H) and $CD8^+$ T_{EM} (Fig. 8I and J) cells in the LCPN@CCD and LCPN@CCD + CAR-T groups was obviously greater than that in the control group ($P < 0.001$), confirming that mice treated with LCPN@CCD and LCPN@CCD + CAR-T formed long-term immune memory. Together, these results suggest that LCPN@CCD or LCPN@CCD + CAR-T cells have long-term antitumor effects on mice and strong antitumor activity *in vivo*.

4. Conclusions

This study prepared LCPN@ACD can achieve effective expression of tumor antigen on the tumor cell membrane, downregulate tumor cell CD55, and induce ICD effect. Both *in vivo* and *in vitro* experiments have confirmed that LCPN@ACD restored tumor MHC-I/antigen expression and T-cell recognition, silenced tumor cell CD55 to increase the $ICOSL^+$ B-cell proportion, and enhanced T-cell activation through the ICD effect. The TIME after LCPN@ACD treatment was greatly relieved, which in turn greatly improved the immunotherapy effect of aPD-1 and CAR-T therapies. In summary, we have started a new exploration that directly edits tumor cells to reverse tumor immune escape at the root. It can provide new inspiration for immunotherapy that involves T cells, including immune checkpoint blockade therapy, adoptive cell therapy, tumor vaccines, etc.

Acknowledgments

Our work was supported by the National Natural Science Foundation of China (82173757, 81974498, 82173756), the Natural Science Foundation of Shandong Province (ZR2023QH285, China), the Innovation Team of Shandong Higher School Youth Innovation Technology Program (2022KJ197, China) and Talent Introduction (Promotion) Program of Shandong First Medical University & Shandong Academy of Medical Sciences. Here, the authors would like to express our heartfelt thanks to the Translational Medicine Core Facility of Shandong University for the technical support provided to this project. The authors appreciate the Pharmaceutical Biology sharing platform of Shandong University for supporting the cell-related experiments. We thank the support provided by BioRender.com in creating Fig. 1 (Agreement number: TW25OJVTP0).

Author contributions

Shujun Liu: Conceptualization, Data curation, Investigation, Methodology, Software, Validation, Writing − original draft. Shijun Yuan: Data curation, Investigation, Methodology, Software, Visualization, Writing − original draft, Writing − review & editing. Meichen Liu: Investigation, Methodology. Jinhu Liu: Investigation, Methodology. Shunli Fu: Validation, Visualization. Tong Gao: Software, Validation, Visualization. Shuang Liang: Methodology, Software. Xinyan Huang: Methodology. Xinke Zhang: Software. Yongjun Liu: Funding acquisition. Zipeng Zhang: Conceptualization, Funding acquisition, Writing − review & editing. Na Zhang: Conceptualization, Funding acquisition, Writing − review & editing.

Conflicts of interest

The authors have no conflicts of interest to declare.

Appendix A. Supporting information

Supporting information to this article can be found online at https://doi.org/10.1016/j.apsb.2024.08.028.

References

1. Saez-Ibañez AR, Upadhaya S, Partridge T, Shah M, Correa D, Campbell J. Landscape of cancer cell therapies: trends and real-world data. *Nat Rev Drug Discov* 2022;**21**:631−2.
2. Scott EC, Baines AC, Gong Y, Moore R, Jr Pamuk GE, Saber H, et al. Trends in the approval of cancer therapies by the FDA in the twenty-first century. *Nat Rev Drug Discov* 2023;**22**:625−40.
3. Ahmad A, Khan P, Rehman AU, Batra SK, Nasser MW. Immunotherapy: an emerging modality to checkmate brain metastasis. *Mol Cancer* 2023;**22**:111.
4. Ye F, Dewanjee S, Li Y, Jha NK, Chen ZS, Kumar A, et al. Advancements in clinical aspects of targeted therapy and immunotherapy in breast cancer. *Mol Cancer* 2023;**22**:105.
5. Hong M, Chen YY. Killer fatigue: transition to NK-cell-like phenotype is a signature of CAR-T cell exhaustion. *Cell* 2021;**184**:6017−9.
6. Carnevale J, Shifrut E, Kale N, Nyberg WA, Blaeschke F, Chen YY, et al. RASA2 ablation in T cells boosts antigen sensitivity and long-term function. *Nature* 2022;**609**:174−82.
7. Wagner DL, Fritsche E, Pulsipher MA, Ahmed N, Hamieh M, Hegde M, et al. Immunogenicity of CAR T cells in cancer therapy. *Nat Rev Clin Oncol* 2021;**18**:379−93.
8. Lim WA, June CH. The principles of engineering immune cells to treat cancer. *Cell* 2017;**168**:724−40.
9. Riaz N, Havel JJ, Makarov V, Desrichard A, Urba WJ, Sims JS, et al. Tumor and microenvironment evolution during immunotherapy with nivolumab. *Cell* 2017;**171**. 934-49.e16.
10. Jhunjhunwala S, Hammer C, Delamarre L. Antigen presentation in cancer: insights into tumour immunogenicity and immune evasion. *Nat Rev Cancer* 2021;**21**:298−312.
11. Adamik J, Butterfield LH. What's next for cancer vaccines. *Sci Transl Med* 2022;**14**:eabo4632.
12. Gu SS, Zhang W, Wang X, Jiang P, Traugh N, Li Z, et al. Therapeutically increasing MHC-I expression potentiates immune checkpoint blockade. *Cancer Discov* 2021;**11**:1524−41.
13. Yamamoto K, Venida A, Yano J, Biancur DE, Kakiuchi M, Gupta S, et al. Autophagy promotes immune evasion of pancreatic cancer by degrading MHC-I. *Nature* 2020;**581**:100−5.
14. Kalbasi A, Tariveranmoshabad M, Hakimi K, Kremer S, Campbell KM, Funes JM, et al. Uncoupling interferon signaling and antigen presentation to overcome immunotherapy resistance due to JAK1 loss in melanoma. *Sci Transl Med* 2020;**12**:eabb0152.
15. Hou AJ, Chen LC, Chen YY. Navigating CAR-T cells through the solid-tumour microenvironment. *Nat Rev Drug Discov* 2021;**20**:531−50.
16. Liu T, Liu C, Yan M, Zhang L, Zhang J, Xiao M, et al. Single cell profiling of primary and paired metastatic lymph node tumors in breast cancer patients. *Nat Commun* 2022;**13**:6823.
17. Chao Y, Liu Z. Biomaterials tools to modulate the tumour microenvironment in immunotherapy. *Nat Rev Bioeng* 2023;**1**:125−38.
18. Yadav M, Jhunjhunwala S, Phung QT, Lupardus P, Tanguay J, Bumbaca S, et al. Predicting immunogenic tumour mutations by combining mass spectrometry and exome sequencing. *Nature* 2014;**515**:572−6.
19. Mantovani A, Marchesi F, Jaillon S, Garlanda C, Allavena P. Tumor-associated myeloid cells: diversity and therapeutic targeting. *Cell Mol Immunol* 2021;**18**:566−78.
20. Maskalenko NA, Zhigarev D, Campbell KS. Harnessing natural killer cells for cancer immunotherapy: dispatching the first responders. *Nat Rev Drug Discov* 2022;**21**:559−77.
21. Tyrakis PA, Palazon A, Macias D, Lee KL, Phan AT, Veliça P, et al. *S*-2-Hydroxyglutarate regulates CD8(+) T-lymphocyte fate. *Nature* 2016;**540**:236−41.
22. Lu Y, Zhao Q, Liao JY, Song E, Xia Q, Pan J, et al. Complement signals determine opposite effects of B cells in chemotherapy-induced immunity. *Cell* 2020;**180**. 1081-97.e24.
23. Helmink BA, Reddy SM, Gao J, Zhang S, Basar R, Thakur R, et al. B cells and tertiary lymphoid structures promote immunotherapy response. *Nature* 2020;**577**:549−55.
24. Petitprez F, de Reyniès A, Keung EZ, Chen TW, Sun CM, Calderaro J, et al. B cells are associated with survival and immunotherapy response in sarcoma. *Nature* 2020;**577**:556−60.
25. Wang SS, Liu W, Ly D, Xu H, Qu L, Zhang L. Tumor-infiltrating B cells: their role and application in anti-tumor immunity in lung cancer. *Cel Mol Immunol* 2019;**16**:6−18.
26. Guan L, Zhang Z, Gao T, Fu S, Mu W, Liang S, et al. Depleting tumor infiltrating B cells to boost antitumor immunity with tumor immune-microenvironment reshaped hybrid nanocage. *ACS Nano* 2022;**16**:4263−77.
27. Liu Z, Fu YX. Chemotherapy induces cancer-fighting B cells. *Cell* 2020;**180**:1037−9.
28. Kroemer G, Galassi C, Zitvogel L, Galluzzi L. Immunogenic cell stress and death. *Nat Immunol* 2022;**23**:487−500.
29. Sun Q, Zhou Z, Qiu N, Shen Y. Rational Design of cancer nanomedicine: nanoproperty integration and synchronization. *Adv Mater* 2017;**29**.
30. Wu W, Pu Y, Shi J. Dual size/charge-switchable nanocatalytic medicine for deep tumor therapy. *Adv Sci* 2021;**8**:2002816.
31. Marciscano AE, Anandasabapathy N. The role of dendritic cells in cancer and anti-tumor immunity. *Semin Immunol* 2021;**52**:101481.
32. Zhang X, Wu Y, Lin J, Lu S, Lu X, Cheng A, et al. Insights into therapeutic peptides in the cancer-immunity cycle: update and challenges. *Acta Pharm Sin B* 2024.

33. Guo Y, Wang SZ, Zhang X, Jia H-R, Zhu YX, Zhang X, et al. *In situ* generation of micrometer-sized tumor cell-derived vesicles as autologous cancer vaccines for boosting systemic immune responses. *Nat Commun* 2022;**13**:6534.

34. Elzoghby AO, Samir O, Emam HE, Soliman A, Abdelgalil RM, Elmorshedy YM, et al. Engineering nanomedicines for immunogenic eradication of cancer cells: recent trends and synergistic approaches. *Acta Pharm Sin B* 2024;**14**:2475−504.